nature physics

ARTICLES

PUBLISHED ONLINE: 6 FEBRUARY 2011 | DOI: 10.1038/NPHYS1908

Observation of ordered vortices with Andreev bound states in $Ba_{0.6}K_{0.4}Fe_2As_2$

Lei Shan[1]*, Yong-Lei Wang[1], Bing Shen[1], Bin Zeng[1], Yan Huang[1], Ang Li[2], Da Wang[3], Huan Yang[1], Cong Ren[1], Qiang-Hua Wang[3], Shuheng H. Pan[2] and Hai-Hu Wen[1,3]*

For a type-II superconductor in an applied magnetic field greater than the lower critical field H_{c1}, the magnetic flux will penetrate into the superconductor and form quantized vortices with Andreev bound states in the vortex cores. The characteristics of the bound states are related to the pairing symmetry and band structure of the superconductor. Recently, a new family of high temperature (high-T_c) superconductors, the iron pnictides, has been discovered. Surprisingly, in electron-doped $Ba(Fe_{1-x}Co_x)_2As_2$, no bound state was found in the vortices. Here, we use a low-temperature scanning tunnelling microscope to study the electronic structure of hole-doped $Ba_{0.6}K_{0.4}Fe_2As_2$. Two superconducting gaps (with gap values $2\Delta/k_BT_c \approx 2.2$ and 5.1, where k_B is Boltzmann's constant) were observed in the superconducting state. By applying magnetic fields, we observed ordered vortices with Andreev bound states in the vortex cores. The bound states and their spatial evolution can be qualitatively explained by our numerical calculations for multiband *s*-wave superconductivity.

As a new family of high-T_c superconductor (HTSCs) in addition to the well known cuprates, iron pnictides have attracted great interest recently in the field of condensed matter physics[1]. On the one hand, Mazin *et al.*[2] suggested theoretically that iron pnictides might have an $s\pm$ pairing, the so-called extended *s*-wave pairing with opposite signs of the order parameters between the hole pockets and the electron pockets. This is different from both conventional *s*-wave superconductors and *d*-wave HTSCs, and has not yet been observed in nature. On the other hand, although the well known Andreev bound states have been predicted and observed in the vortex cores of conventional type-II superconductors[3–7], they have still not been demonstrated beyond doubt in multi-gap superconductors (such as MgB_2) or HTSCs. Iron pnictides provide a particular opportunity to study the vortex physics in multi-band high T_c superconductors. According to the $s\pm$ pairing model mentioned above, the iron pnictides might have multiple nodeless superconducting gaps and, more attractively, they could exhibit asymmetric Andreev bound states in the vortex cores[8], as can be verified by measurements using a low-temperature scanning tunnelling microscope (STM; ref. 9). Surprisingly, the previous STM measurements on iron pnictides always detected a single superconducting gap with remarkable zero-bias conductance. In addition, although the recent STM data for an electron-doped iron pnictide superconductor $Ba(Fe_{1-x}Co_x)_2As_2$ (ref. 10) successfully demonstrated the observation of disordered magnetic vortices[11,12], no Andreev bound state has been observed in the vortex cores. This result has also been confirmed by another STM group (S. H. Pan *et al.*, unpublished). Apparently, the available results of STM data[10,13–18] are still too limited to reach a consensus. An intriguing question we can pose is, for the hole-doped pnictides, can we observe multiple gaps in the superconducting state and the theoretically predicted Andreev bound states in the vortex cores?

To solve these puzzles, we decided to perform low-temperature STM measurements on the iron pnictide superconductor $Ba_{1-x}K_xFe_2As_2$, which is hole-doped from the same parent compound $BaFe_2As_2$ used for the electron-doped sample studied in the previous STM experiments[10]. The $Ba_{0.6}K_{0.4}Fe_2As_2$ single crystals ($T_c = 38$ K) used in our experiments were grown by the self-flux method (see the Methods section). The samples were cold-cleaved *in situ* of the STM chamber, then immediately inserted into the microscope, which was already at the desired temperature. It is known that cleaving layered compounds may provoke charge redistribution, thus affecting the doping level of the surface (polar surfaces). This cannot be distinguished by STM, although the angle-resolved photon emission spectroscopy (ARPES) data obtained on the cleaved surface of the same samples gives the expected doping level[19], indicating that the polar effect is not a serious issue. Here, we report the study of spatially resolved tunnelling spectroscopy on $Ba_{0.6}K_{0.4}Fe_2As_2$. We observed two superconducting gaps and, most interestingly, vortex bound states in the quantum limit, which can be well understood in the framework of the $s\pm$ pairing model.

Figure 1a shows a typical topographic image of the *in situ*-cleaved $Ba_{0.6}K_{0.4}Fe_2As_2$. Most of the spectra measured on such surfaces exhibit clear superconducting gaps. However, it was found that the tip tends to become contaminated by atomic clusters picked up from these surfaces or induces a local topographic modification in the scanning process. This inhibits us from successfully performing spectroscopic mapping over a sufficiently large area and thus imaging vortices. Fortunately, we could also obtain another type of surface that was hardly modified by the STM tip during the scanning, thus allowing us to obtain reproducible topographic images and to subsequently perform spatially resolved spectroscopic measurements. Figure 1b shows an image obtained under such circumstances. In the field of

[1]National Laboratory for Superconductivity, Institute of Physics and National Laboratory for Condensed Matter Physics, Chinese Academy of Sciences, Beijing 100190, China, [2]Department of Physics and Texas Center for Superconductivity, University of Houston, Houston, Texas 77204-5002, USA, [3]National Laboratory of Solid State Microstructures and Department of Physics, Nanjing University, Nanjing 210093, China.
*e-mail: lshan@aphy.iphy.ac.cn; hhwen@aphy.iphy.ac.cn.

© 2011 Macmillan Publishers Limited. All rights reserved

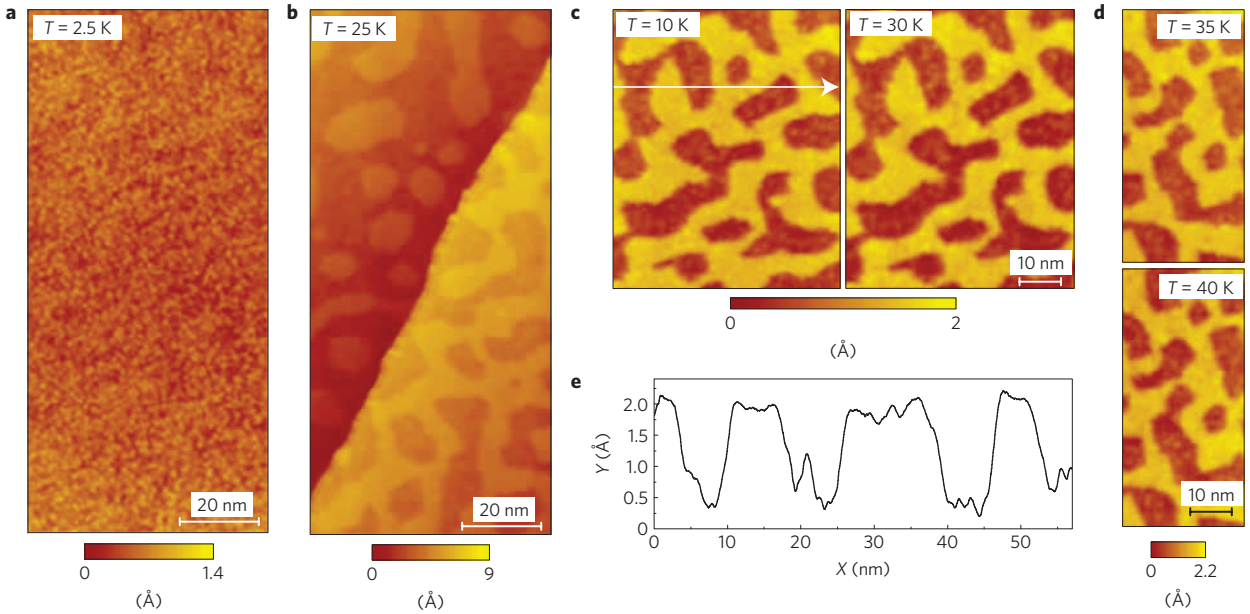

Figure 1 | Topographic STM image of the $Ba_{0.6}K_{0.4}Fe_2As_2$ single crystal cleaved *in situ*. **a**, STM image taken with a sample-bias voltage of $V_s = 50$ mV and tunnelling current of $I_t = 200$ pA. **b**, STM image of another type of cleaved surface taken with $V_s = 100$ mV and $I_t = 40$ pA. **c**,**d**, STM images taken on the same surface as shown in **b** at various temperatures. No change of the surface topography was observed from low temperature to above T_c (38 K). **e**, Section profile along the white line drawn in **c** which spans both bright and dark areas.

view, a half unit-cell step separates the lower cleaved surface from the upper one. It can be seen that both upper and lower surfaces have a similar pattern with interlaced bright and dark domains. Such surface topography can persist up to temperatures above T_c, as shown in Fig. 1c and d. Figure 1e displays a line profile, in terms of height variation, obtained along the white line marked in Fig. 1c. As the constant-current topographic image signal convolutes information about the variations of both the spatial height and the integrated density of states (DOS), it is not possible to identify the origin of such domain-like surfaces merely based on topographic images without atomic resolution. However, spatially resolved tunnelling spectra from the bright and dark regions indeed show some differences.

In Fig. 2b and c we display two sets of tunnelling spectra of $g(V) = dI/dV \propto$ DOS measured respectively along the long and short white lines indicated in Fig. 2a (for the details of measuring $g(V)$, see the Methods section). All curves exhibit superconducting gaps around 4 meV as determined from coherence peaks. The spectra are very homogeneous within an individual bright or dark domain, but differences between the two kinds of domains are noticeable. In general, the gap magnitude is a little smaller and the zero-bias conductance (ZBC) is higher in the dark region. To illustrate the correlation more clearly, we measured a spectroscopic map on a region covering several boundaries of bright and dark domains, as shown in Fig. 3a. The gap magnitude and the zero-bias conductance in the same area are presented in Fig. 3b and c, respectively. It is obvious that the bright domains have larger gaps and lower ZBC than those of the dark area. The anti-correlation strength of the gap magnitude and ZBC is shown in Fig. 3d, and the correlation length is estimated to be 3.7 nm. In Fig. 3e, a typical spectrum from the bright region is compared in detail with the one from the dark region. In addition to the ~4 meV gap, a larger gap of ~8 meV can be identified in the spectrum of the bright region, whereas this two-gap feature is almost invisible in the spectrum taken in the dark region. Figure 3f shows the gap distribution determined by a statistical analysis of more than 1,000 spectra. Two separate gaps can clearly be seen, centred at 3.6 meV and 8.1 meV with Gaussian distribution widths of 0.5 meV and 0.9 meV, respectively. These gap

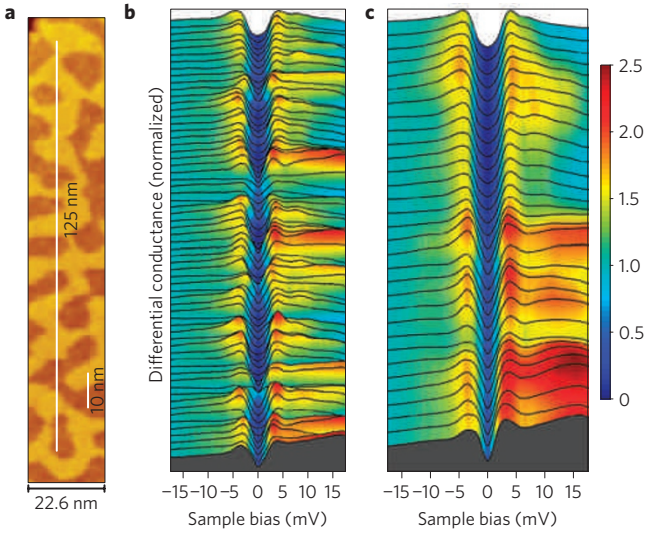

Figure 2 | Spatially resolved spectra in zero magnetic field at 2 K. **a**, Topographic image of $Ba_{0.6}K_{0.4}Fe_2As_2$ taken at 2 K. **b**, Differential conductance normalized to the value at −17.5 mV versus bias voltage (dI/dV spectra) measured along the trajectory with a length of 125 nm drawn in **a** (the longer white line). **c**, A series of dI/dV spectra taken along a 10 nm line indicated by the shorter line in **a**, illustrating the variation of gap magnitude when crossing the boundary between bright and dark areas. The spectra were recorded with the settings: $V_s = 100$ mV, $I_t = 200$ pA for **b** and $V_s = 20$ mV, $I_t = 500$ pA for **c**.

values are roughly consistent with those (around 2 meV and 9 meV) obtained in our H_{c1} measurements[20]. The corresponding gap ratios of $2\Delta/k_BT_c \approx 2.2$ and 5.1 are respectively much smaller and much larger than the predicted value of 3.53 in the weak-coupling BCS theory. However, they are close to some recent ARPES results, for example, <3 and 6.8 (ref. 21) or 2.4 and 4.4 (ref. 22). Another new finding here is that many of the tunnelling spectra from the bright region show negligible ZBC compared to that of the Co-doped

© 2011 Macmillan Publishers Limited. All rights reserved

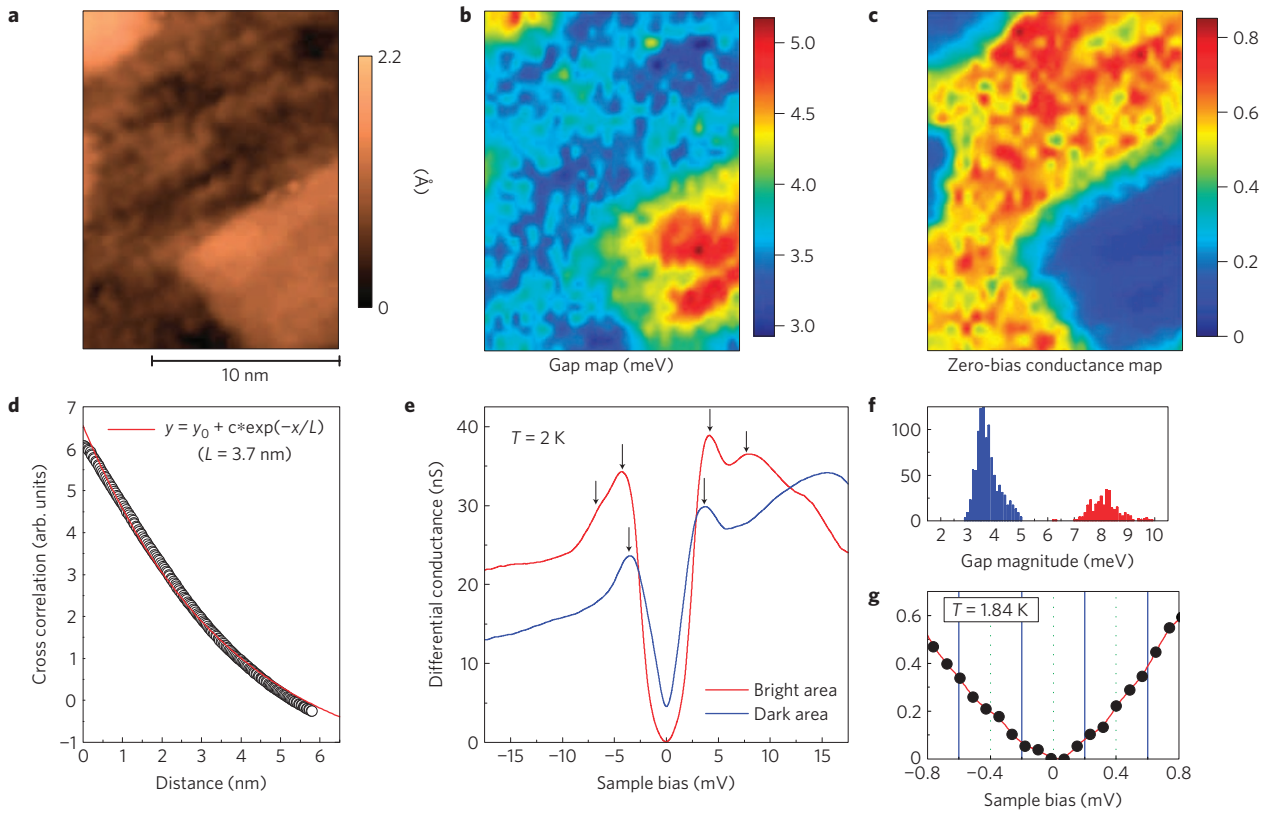

Figure 3 | Comparison between the bright and dark areas. a, A 14 × 18 nm^2 topographic image covering both bright and dark areas. **b**, Gap map of the same region presented in **a**, showing the spatial variation of the gap magnitude for the dominant gap (that is, the smaller one). **c**, A ZBC map obtained in the same region presented in **a** and **b**. The data are normalized to the value measured at a bias of −17.5 mV for every pixel. **d**, The strength of the anti-correlation of the gap magnitude (as shown in **b**) and ZBC (as shown in **c**), the correlation length is estimated to be $L = 3.7$ nm by fitting to the exponential decay law indicated by the red line. **e**, Two dI/dV spectra measured in bright and dark areas, respectively. The gap magnitudes can be estimated from the coherence peaks indicated by the black arrows. **f**, A histogram of the superconducting gaps counted for more than 1,000 spectra. **g**, The details of the low-bias part of the spectrum measured in the bright area.

$BaFe_2As_2$ compound[10]. Figure 3g shows a zoomed-in spectrum at low bias, again exhibiting the vanishingly small conductance around zero bias. To get a quantitative understanding of the ZBC, we attempted some calculations using a simplified two-gap model with various gap symmetries to fit the experimental data. In the calculations, the tunnelling current is expressed by

$$I_{S(L)}(V) = \frac{1}{2\pi}\int_{-\infty}^{\infty} d\varepsilon \int_0^{2\pi} d\theta \left[f(\varepsilon) - f(\varepsilon + eV)\right] \times \mathrm{Re}\left(\frac{\varepsilon + eV + i\Gamma_{S(L)}}{\sqrt{(\varepsilon + eV + i\Gamma_{S(L)})^2 - \Delta_{S(L)}^2(\theta)}}\right) \quad (1)$$

where f is a Fermi function taking into account the thermal broadening, the subscript S(L) indicates the smaller gap (resp. larger gap) and $\Gamma_{S(L)}$ represents the scattering rate for quasiparticles[23]. The overall conductance is obtained by a linear combination of two components $g(V) = P(dI_S/dV) + (1-P)(dI_L/dV)$ in which P is the spectral weight contributed by the smaller gap. Here, we take the gap function $\Delta_{S(L)}{}^{nodeless}(\theta) = \Delta_{S(L)}{}^0[0.3\cos(2\theta) + 0.7]$ to simulate nodeless gaps and $\Delta_{S(L)}{}^{nodal}(\theta) = \Delta_{S(L)}{}^0\cos(2\theta)$ to simulate gaps with line nodes. Four possible combinations of $\Delta_{S(L)}{}^{nodeless}(\theta)$ and $\Delta_{S(L)}{}^{nodal}(\theta)$ were tried, all of which could simulate the high-bias part of the spectrum (above 2.5 mV) with the parameters $P \approx 80\%$, $\Delta_S{}^0 \approx 4.2$ meV and $\Delta_L{}^0 \approx 8.0$ meV, regardless of the form of the gap functions, as shown in Fig. 4. However, the shape of the spectrum at low bias around zero depends strongly on the selection of nodal or nodeless gaps. Figure 4a shows the calculations (with the parameters determined above) using the gap functions $\Delta_S{}^{nodeless}(\theta)$, $\Delta_L{}^{nodeless}(\theta)$ (blue line) and $\Delta_S{}^{nodal}(\theta)$, $\Delta_L{}^{nodeless}(\theta)$ (red line), without the effects of scattering ($\Gamma_{S(L)} = 0$). It can be seen that the line nodes in the smaller gap induce an enhancement of conductance at low bias, whereas the nodeless gaps fit the data much better. Line nodes, if assumed to be on the larger gap, can also induce finite low-bias conductance. However, as the contribution given by the larger gap to the total conductance is weak (only 20%), the enhanced conductance is almost beyond the resolution of the measurements. Figure 4b shows the calculations with effective scattering rates of $\Gamma_S = 0.04(\varepsilon + eV)$ and $\Gamma_L = 0.025(\varepsilon + eV)$ (ref. 24). It is obvious that the fit with a nodeless gap is improved, whereas that with a nodal gap is not. Nonetheless, considering the complicated Fermi surfaces and the limit of experimental resolution, we cannot exclude the existence of a slight contribution from 'accidental' nodes[25] possibly located on some segments of the Fermi surfaces. It also needs to be pointed out that not all the spectra from the bright region show zero conductance near the Fermi energy. This can probably be attributed to some low-energy quasiparticle excitations due to, for example, impurity scattering. In this sense, the smaller gap size and the much higher ZBC observed in the spectra from the dark regions may be attributed to stronger disorder-induced scattering on the surfaces of these domains.

To image vortices, we take a ZBC map simultaneously as we record the surface topography. Figure 5a shows such a conductance map recorded in a magnetic field of 9 T. Another conductance map

© 2011 Macmillan Publishers Limited. All rights reserved

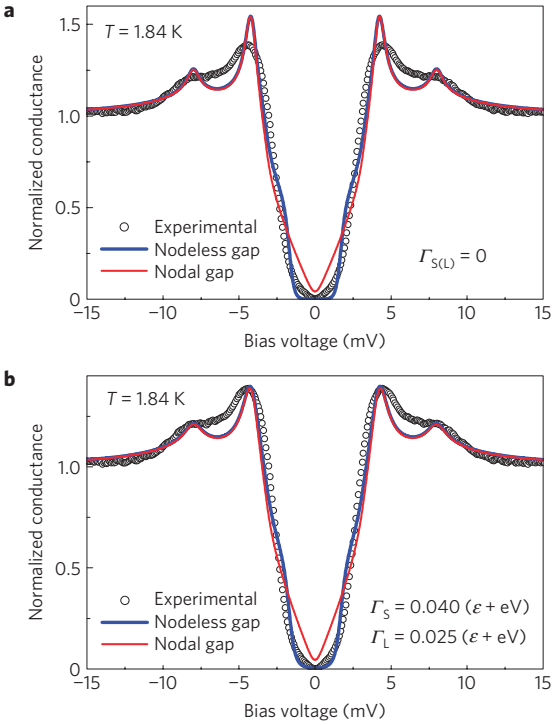

Figure 4 | Fitting experimental data to a two-gap model with a larger superconducting gap $\Delta_L(\theta)$ and a smaller one $\Delta_S(\theta)$. a, Fitting with $\Delta_L(\theta) = 8 \cdot [0.3\cos(2\theta) + 0.7]$, the blue line and the red one correspond to $\Delta_S(\theta) = 4.2 \cdot [0.3\cos(2\theta) + 0.7]$ and $\Delta_S(\theta) = 4.2 \cdot \cos(2\theta)$, respectively. **b**, Fitting with the same gap functions as in **a** while taking into account an effective scattering rate ($\Gamma_{S(L)}$) for quasiparticles.

recorded at 4 T is shown in Fig. 5c. In both maps, with a resolution of 64 × 128 pixels (without any filtering), the vortices appear as the loci with enhanced DOS. The average flux per vortex is about 2.17×10^{-15} Wb at 9 T and 1.98×10^{-15} Wb at 4 T, consistent with the single magnetic flux quantum $\phi_0 = 2.07 \times 10^{-15}$ Wb. In the simultaneously obtained topographic images shown in Fig. 5b and d, the vortex positions are marked as blue circles. Figure 5e and f show the self-correlation and Fourier transform analyses of the observed vortices. A slight distorted hexagonal order can be seen clearly for both fields. As the maximal scanning area is limited, we cannot identify whether the observed hexagonal structure is just a locally ordered state or it has a long range order. Interestingly, by drawing a circle with a diameter of 25 Å to cover a vortex region, we can find that more than 70% of the circles (vortices) will touch or intersect the boundaries of the bright and dark domains (or the step on the surface). Such surface pinning is possibly responsible for the slight distortion of the hexagonal order.

A single vortex image on a scale of 78 Å × 104 Å is shown in Fig. 6a with a resolution of 32 × 32 pixels; the enhancement of ZBC around the vortex centre is remarkable. To reveal the vortex-induced variation of local DOS, 64 spectra (dI/dV) were taken equally spaced along a 104 Å line (with an interval of 1.6 Å) crossing the vortex as denoted in Fig. 6a. The locus of the studied vortex and the measured trajectory are marked as the black dot and line in the topographic image (Fig. 6b) for clarity. The obtained data are presented in Fig. 6c. At the vortex centre, a remarkable conductance peak dominates the line shape of the spectrum. The peak is not exactly at zero bias, instead, it is located at a finite negative bias of about −0.5 mV. This negative-bias conductance peak splits into two peaks when measured at more than 6.4 Å away from vortex centre, with a dominant spectral weight at negative bias. Finally, the two-peak feature disappears and the spectrum evolves continuously into the zero-field one. To highlight this systematic evolution, we show in Fig. 6d the spectra taken at some typical positions symmetric about the vortex centre. The asymmetrically split peaks are indicated by short grey bars. To extract the superconducting coherence length ξ, the radial dependences of the vortex-induced ZBC measured along various azimuthal angles are normalized to unity at $r = 0$ (vortex centre) and plotted together in Fig. 6e. Then an exponential decay law of $g(r, V = 0) = g_\infty + A\exp(-r/\xi)$ is fitted to the data between $r = 10$ Å and $r = 50$ Å. From several vortices, we find an average coherence length $\xi = 21 \pm 3$ Å. With the Ginzburg–Landau expression $H_{c2} = \phi_0/2\pi\xi^2$, the upper critical field H_{c2} is estimated to be 75 T, which is higher than that of the

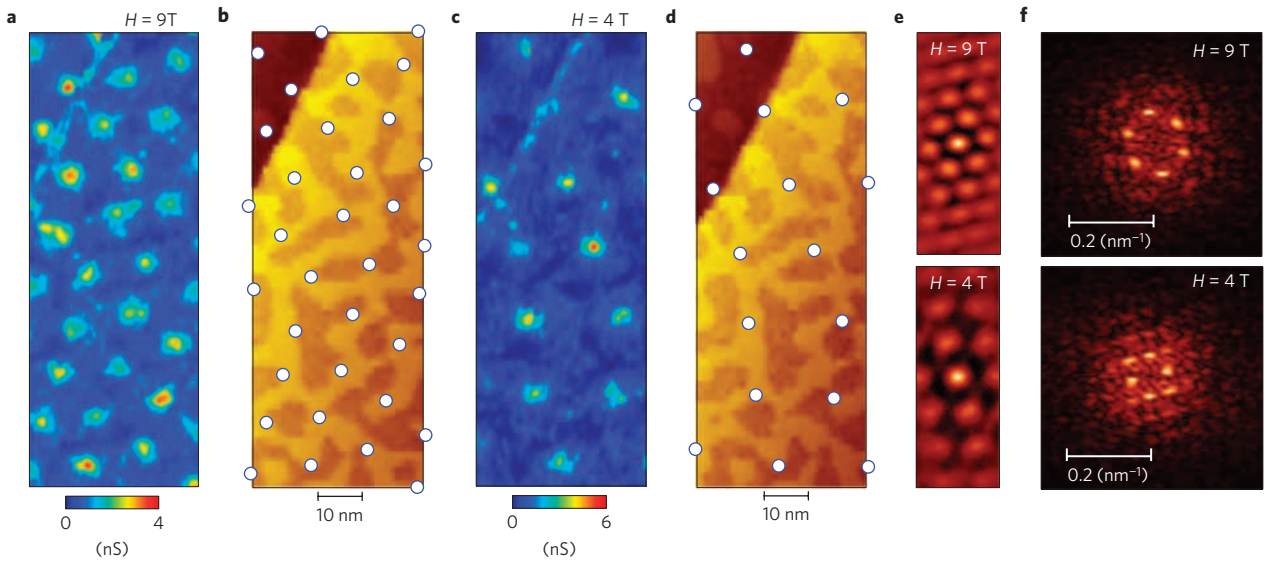

Figure 5 | Vortex lattice observed in $Ba_{0.6}K_{0.4}Fe_2As_2$ at 2 K. a, A 130 nm × 50 nm ZBC map recorded at a magnetic field of 9 T with the settings: $V_s = 100$ mV, $I_t = 200$ pA. **b**, Topographic image recorded simultaneously with the map in **a**, the vortex positions derived from **a** are denoted by blue circles. **c**, A ZBC map measured under a magnetic field of 4T. **d**, Topographic image recorded simultaneously with the map in **c**, vortex positions are denoted by blue circles. **e**, Self-correlation analysis for the vortex images shown in **a** and **c**. **f**, Two-dimensional Fourier transformation for the vortex images. A hexagonal order with slight distortion is obvious in both **e** and **f**.

© 2011 Macmillan Publishers Limited. All rights reserved

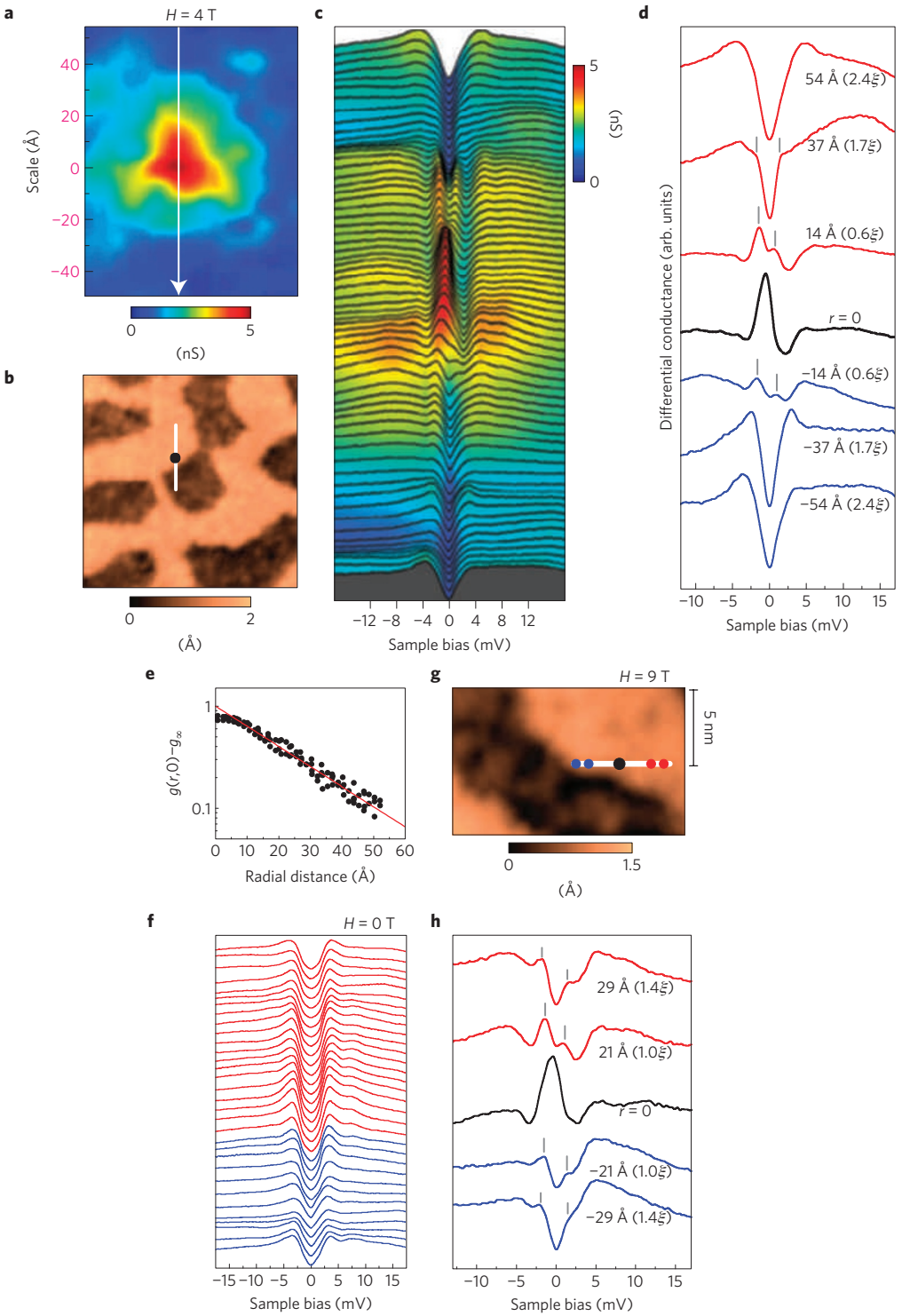

Figure 6 | Vortex core states of $Ba_{0.6}K_{0.4}Fe_2As_2$, all spectra were taken at 2 K. a, A 104 Å × 78 Å ZBC map around a single vortex measured at 4 T with the settings: $V_s = 100$ mV, $I_t = 200$ pA. **b**, Topographic background (34.5×34.5 nm^2) where the vortex shown in **a** is imaged. The white line is identical with that shown in **a** and the black dot indicates the vortex centre. **c**, The 64 spectra taken along a 104 Å trajectory (white lines indicated in **a** and **b**) through the vortex. **d**, Enlarged view of the spectra for some particular positions, the distance r from the vortex centre is indicated. **e**, Radial dependence of ZBC ($g(r,0) - g_\infty$) around a single vortex and fitted to an exponential decay (g_∞ is the constant background). The fit leads to a coherence length $\xi = 22 \pm 1.7$ Å. **f**, A series of spectra measured in zero field along the same trajectory as that in **c** for comparison. **g**, Topographic background where another vortex is imaged. The black dot indicates the vortex centre. Some particular positions symmetric about the vortex centre are indicated by the blue dots (close to the dark area) and red dots (far away from the dark area). **h**, The spectra taken at the positions denoted by the dots presented in **g**.

underdoped $Ba_{1-x}K_xFe_2As_2$ (below 70 T; ref. 26) and the optimally doped $Ba(Fe_{1-x}Co_x)_2As_2$ (43 T; ref. 10). As presented in Fig. 6f, we have also measured spectra at zero field along the same line as shown in Fig. 6a and b. It is obvious that no additional feature to a clean gap structure can be seen, demonstrating that the observed DOS modulation in the field is truly due to the vortex state instead

© 2011 Macmillan Publishers Limited. All rights reserved

of other factors such as impurity states. We must emphasize that this negative-bias conductance peak is a common feature of all measured vortices. It is noted in Fig. 6c and d that the split peaks are a little stronger in the upper part of the vortex. According to the topography shown in Fig. 6b, it indicates that the peaks are weakened in the dark domains and around the boundaries. Such a correlation between the peak intensity and the surface topography can be verified easily because most of the observed vortices are located near the boundaries. As an example, we show another vortex centred at the black dot indicated in Fig. 6g measured at 9 T. In Fig. 6h, we compare the spectra measured at various positions (marked by the coloured dots in Fig. 6g) symmetric about the vortex centre. It is clear that the split peaks observed inside the bright domain (upper two curves) are much stronger than those recorded around the boundary (lower two curves). As the gap magnitude and the ZBC (or the zero-energy DOS) are also correlated with the domain structure (refer to Fig. 3a–d), it is demonstrated again that the vortex bound states observed here are indeed related to superconductivity.

The existence of the pronounced vortex core bound states peaking at negative bias and the spatial evolution have never been observed previously in other systems. It is in striking contrast to the case of cuprates, in which two weak subgap peaks were observed in the vortex cores[27–31]. At first glance, our observations are very similar to what has been observed in the conventional superconductor 2H-$NbSe_2$ (refs 4,6). The difference is that the bound states observed here in $Ba_{0.6}K_{0.4}Fe_2As_2$ are very asymmetric with respect to the Fermi energy. Actually, asymmetric vortex bound states have been predicted for an *s*-wave superconductor in the quantum limit (that is, $T/T_c \leq 1/(k_F\xi)$; ref. 32) and were demonstrated later in YNi_2B_2C (ref. 33). Combining $\xi \approx 21$ Å derived in our present work with $k_F \approx 0.4$ Å^{-1} (ref. 19), we find that the upper boundary of the quantum limit in our sample is about 4.4 K, so the measurements at 2 K indeed satisfy the quantum limit. According to the formula $E_{1/2}/\Delta_0 = (0.5/k_F\xi)\ln(k_F\xi/0.3)$ (ref. 32), we could roughly estimate the lowest energy level of the quantum-limit bound states to be $E_{1/2} \approx 0.7$ meV, which is close to the absolute value of 0.5 meV observed here. However, the vortex core states reported in refs 32,33 contribute a dominant peak at a positive bias in contrast to the negative one observed here. It is also very intriguing that the prominent vortex bound states in $Ba_{0.6}K_{0.4}Fe_2As_2$ have not been observed in $Ba(Fe_{1-x}Co_x)_2As_2$ (ref. 10). This discrepancy may be attributed to the stronger scattering by the in-plane Co-dopants in $Ba(Fe_{1-x}Co_x)_2As_2$. Alternatively, it might be due to the multiband superconductivity in iron pnictides, where the classical treatment of vortex core bound states may not be valid.

To get a further insight into this issue, we have performed large-scale numerical calculations for the vortex state using a two-orbit tight-binding model (for details, see Supplementary Information). The negative-biased bound state, the peak splitting and merging to the gap edges away from vortex core are qualitatively visualized for both in-phase and anti-phase *s*-wave pairing (s++ and $s\pm$). A non-zero energy level is a manifestation of the quantum limit of the Caroli–de Gennes bound states[3,32]. The asymmetry is realized when the coherence length is of the order of the Fermi wavelength, or in other words, when the Fermi level is close to the band edge so that the normal state band spectra is asymmetric with respect to the Fermi level. Indeed, in the model under consideration and from ARPES, the Fermi level is close to the top of the hole-like bands.

Combining the measured multiple gaps with the numerical calculations, we conclude that the asymmetric vortex bound states observed in $Ba_{0.6}K_{0.4}Fe_2As_2$ may originate from the quantum-regime vortex core in this multiband extended *s*-wave superconductor. The calculations suggest that the asymmetry is due to the band-edge effect, but insensitive to the relative phase of the *s*-wave pairing gaps. Quantitative agreement between the experimental and numerical results would require a more refined model that includes contributions from all five orbits. According to the calculations, the vortex core bound states observed in $Ba_{0.6}K_{0.4}Fe_2As_2$ should also be observed in $Ba(Fe_{1-x}Co_x)_2As_2$ if the system is in the clean limit. However, Co-doping into FeAs layers, although it provides charge carriers to achieve superconductivity, also introduces scattering centres in the superconducting layers. Therefore, the bound states could be smeared out in the vortices of in-plane doped $Ba(Fe_{1-x}Co_x)_2As_2$ (ref. 10) whereas surviving in that of the off-plane doped $Ba_{0.6}K_{0.4}Fe_2As_2$. In this sense, the missing conductance peak in the vortex core of $Ba(Fe_{1-x}Co_x)_2As_2$ is similar to the case of a dirty conventional superconductor[9]. Recently, the calculations from a separate group[34] show very good consistency with our data. According to this work, the absence of vortex core bound states in $Ba(Fe_{1-x}Co_x)_2As_2$ may be attributed to the stronger spin density wave order induced within the vortex cores by the magnetic field, compared with the case in $Ba_{0.6}K_{0.4}Fe_2As_2$. This will be an interesting issue for future experiments.

Methods

Sample growth. The $Ba_{0.6}K_{0.4}Fe_2As_2$ single crystals were grown using FeAs as the self-flux. The starting materials Ba, K and FeAs were mixed in a ratio of 0.6:1:4 and filled in a ceramic crucible. The weighing, mixing and pressing procedures were performed in a glove box filled with highly pure Ar gas, and both O_2 and H_2O concentrations were less than 0.1 ppm. The crucible containing the starting materials was sealed in a Ta tube, which was sealed in an evacuated quartz tube. It was heated up to 1,150 °C, maintained for 5 h, then cooled down to 800 °C at a rate of 8 °C h^{-1}. The samples used in this work were 1.5 mm × 1.5 mm × 0.2 mm in size. The superconducting transition temperature determined from zero resistivity is $T_c = 38$ K, with a transition width of about 1 K, and the residual specific heat coefficient γ_0 is about 1.24 mJ K^{-2}mol^{-1} (for details of sample characterization, see Supplementary Information).

Tunnelling spectra measurements. To obtain a tunnelling spectrum at a given location, we hold the tip–sample separation constant and use a lock-in amplifier to modulate the bias voltage by dV (about 0.1–0.2 mV in this work) around a voltage V of interest. Such voltage modulation dV will lead to a current modulation dI at the same frequency that can be measured readily. Therefore, by using a lock-in amplifier and varying the bias voltage V, we can obtain a entire tunnelling spectrum (or a DOS curve), that is, $g(V) = \mathrm{d}I/\mathrm{d}V \propto \mathrm{DOS}$ (eV).

Received 25 May 2010; accepted 16 December 2010; published online 6 February 2011

References

1. Kamihara, Y., Watanabe, T., Hirano, M. & Hosono, H. Iron-based layered superconductor La[$O_{1-x}F_x$]FeAs ($x = 0.05$–0.12) with $T_c = 26$ K. *J. Am. Chem. Soc.* **130,** 3296–3297 (2008).
2. Mazin, I. I., Singh, D. J., Johannes, M. D. & Du, M. H. Unconventional sign-reversing superconductivity in $LaFeAsO_{1-x}F_x$. *Phys. Rev. Lett.* **101,** 057003 (2008).
3. Caroli, C., de Gennes, P. G. & Matricon, J. Bound fermion states on a vortex line in a type II superconductor. *Phys. Lett.* **9,** 307–309 (1964).
4. Hess, H. F., Robinson, R. B., Dynes, R. C., Valles, J. M. Jr & Waszczak, J. V. Scanning-tunnelling-microscope observation of the Abrikosov flux lattice and the density of states near and inside a fluxoid. *Phys. Rev. Lett.* **62,** 214–216 (1989).
5. Shore, J. D., Huang, M., Dorsey, A. T. & Sethna, J. P. Density of states in a vortex core and the zero-bias tunneling peak. *Phys. Rev. Lett.* **62,** 3089–3092 (1989).
6. Hess, H. F., Robinson, R. B. & Waszczak, J. V. Vortex-core structure observed with a scanning tunneling microscope. *Phys. Rev. Lett.* **64,** 2711–2714 (1990).
7. Gygi, F. & Schlüter, M. Electronic tunneling into an isolated vortex in a clean type-II superconductor. *Phys. Rev. B* **41,** 822–825 (1990).
8. Hu, X., Ting, C. S. & Zhu, J. X. Vortex core states in a minimal two-band model for iron-based superconductors. *Phys. Rev. B* **80,** 014523 (2009).
9. Fischer, Ø., Kugler, M., Maggio-Aprile, I., Berthod, C. & Renner, C. Scanning tunneling spectroscopy of high-temperature superconductors. *Rev. Mod. Phys.* **79,** 353–419 (2007).
10. Yin, Y. *et al.* Scanning tunneling spectroscopy and vortex imaging in the iron pnictide superconductor $BaFe_{1.8}Co_{0.2}As_2$. *Phys. Rev. Lett.* **102,** 097002 (2009).
11. Eskildsen, M. R. *et al.* Vortices in superconducting $Ba(Fe_{0.93}Co_{0.07})_2As_2$ studied via small-angle neutron scattering and bitter decoration. *Phys. Rev. B* **79,** 100501(R) (2009).
12. Luan, L. *et al.* Local measurement of penetration depth in the pnictide superconductor $Ba(Fe_{0.95}Co_{0.05})_2As_2$. *Phys. Rev. B* **81,** 100501(R) (2010).

© 2011 Macmillan Publishers Limited. All rights reserved

13. Hanaguri, T., Niitaka, S., Kuroki, K. & Takagi, K. Unconventional *s*-wave superconductivity in Fe(Se, Te). *Science* **328,** 474–476 (2010).
14. Wray, L. *et al.* Momentum dependence of superconducting gap, strong-coupling dispersion kink, and tightly bound Cooper pairs in the high-T_c(Sr, Ba)$_{1-x}$(K, Na)$_x$Fe$_2$As$_2$ superconductors. *Phys. Rev. B* **78,** 184508 (2008).
15. Nascimento, V. B. *et al.* Surface geometric and electronic structure of BaFe$_2$As$_2$(001). *Phys. Rev. Lett.* **103,** 076104 (2009).
16. Niestemski, F. C. *et al.* Unveiling the atomic and electronic structure at the surface of the parent pnictide SrFe$_2$As$_2$. Preprint at http://arxiv.org/abs/0906.2761 (2009).
17. Massee, F. *et al.* Cleavage surfaces of the BaFe$_{2-x}$Co$_x$As$_2$ and Fe$_y$Se$_{1-x}$Te$_x$ superconductors: A combined STM plus LEED study. *Phys. Rev. B* **80,** 140507(R) (2009).
18. Chuang, T-M. *et al.* Nematic electronic structure in the 'parent' state of the iron-based superconductor Ca(Fe$_{1-x}$Co$_x$)$_2$As$_2$. *Science* **327,** 181–184 (2010).
19. Ding, H. *et al.* Observation of Fermi-surface-dependent nodeless superconducting gaps in Ba$_{0.6}$K$_{0.4}$Fe$_2$As$_2$. *Europhys. Lett.* **83,** 47001 (2008).
20. Ren, C. *et al.* Evidence for two energy gaps in superconducting Ba$_{0.6}$K$_{0.4}$Fe$_2$As$_2$ single crystals and the breakdown of the Uemura plot. *Phys. Rev. Lett.* **101,** 257006 (2008).
21. Evtushinsky, D. V. *et al.* Momentum dependence of the superconducting gap in Ba$_{1-x}$K$_x$Fe$_2$As$_2$. *Phys. Rev. B* **79,** 054517 (2009).
22. Zhang, Y. *et al.* Out-of-plane momentum and symmetry-dependent energy gap of the pnictide Ba$_{0.6}$K$_{0.4}$Fe$_2$As$_2$ superconductor revealed by angle-resolved photoemission spectroscopy. *Phys. Rev. Lett.* **105,** 117003 (2010).
23. Dynes, R. C., Garno, J. P., Hertel, G. B. & Orlando, T. P. Tunneling study of superconductivity near the metal–insulator transition. *Phys. Rev. Lett.* **53,** 2437–2440 (1984).
24. Alldredge, J. W. *et al.* Evolution of the electronic excitation spectrum with strongly diminishing hole density in superconducting Bi$_2$Sr$_2$CaCu$_2$O$_{8+\delta}$. *Nature Phys.* **4,** 319–326 (2008).
25. Chubukov, A. V. & Eremin, I. Angle-resolved specific heat in iron-based superconductors: The case for a nodeless extended *s*-wave gap. *Phys. Rev. B* **82,** 060504(R) (2010).
26. Yuan, H. Q. *et al.* Nearly isotropic superconductivity in (Ba, K)Fe$_2$As$_2$. *Nature* **457,** 565–568 (2009).
27. Maggio-Aprile, I., Renner, C., Erb, A., Walker, E. & Fischer, Ø. *et al.* Direct vortex lattice imaging and tunneling spectroscopy of flux lines on YBa$_2$Cu$_3$O$_{7-\delta}$. *Phys. Rev. Lett.* **75,** 2754–2757 (1995).
28. Pan, S. H. *et al.* STM studies of the electronic structure of vortex cores in Bi$_2$Sr$_2$CaCu$_2$O$_{8+\delta}$. *Phys. Rev. Lett.* **85,** 1536–1539 (2000).
29. Hoogenboom, B. W., Renner, C., Revaz, B., Maggio-Aprile, I. & Fischer, Ø. Low-energy structures in vortex core tunneling spectra in Bi$_2$Sr$_2$CaCu$_2$O$_{8+\delta}$. *Physica C* **332,** 440–444 (2000).
30. Shibata, K., Maki, M., Nishizaki, T. & Kobayashi, N. Scanning tunneling spectroscopy studies on vortices in YBa$_2$Cu$_3$O$_y$ single crystals. *Physica C* **392–396,** 323–327 (2003).
31. Levy, G., Kugler, M., Manuel, A. A., Fischer, Ø. & Li, M. Fourfold structure of vortex-core states in Bi$_2$Sr$_2$CaCu$_2$O$_{8+\delta}$. *Phys. Rev. Lett.* **95,** 257005 (2005).
32. Hayashi, N., Isoshima, T., Ichioka, M. & Machida, K. Low-lying quasiparticle excitations around a vortex in quantum limit. *Phys. Rev. Lett.* **80,** 2921–2924 (1998).
33. Nishimori, H. *et al.* First observation of the fourfold-symmetric and quantum regime vortex core in YNi$_2$B$_2$C by scanning tunneling microscopy and spectroscopy. *J. Phys. Soc. Jpn* **73,** 3247–3250 (2004).
34. Gao, Y., Huang, H-X., Chen, C., Ting, C. S. & Su, W-P. Vortex states in hole-doped iron-pnictide superconductors. Preprint at http://arxiv.org/abs/1008.3885 (2010).

Acknowledgements

We thank D. H. Lee, K. Kuroki, T. Xiang and T. Hanaguri for comments and suggestions. This work was supported by the Natural Science Foundation of China (No. 10774170, No. 10974086, No. 10734120), the Ministry of Science and Technology of China (973 Projects No. 2011CBA00100, No. 2011CB922101, No. 2010CB923002), and the Chinese Academy of Sciences.

Author contributions

The low-temperature STM was constructed by L.S., Y-L.W. and Y.H. with the help of S.H.P., A.L. and H-H.W., B.S. and B.Z. prepared the samples and measured the sample quality. L.S. designed and performed STM experiments and analysed data. Y-L.W. performed STM experiments and analysed data. D.W. and Q-H.W. contributed to numerical calculations. H-H.W. coordinated the whole work, contributed to sample preparation, STM experiments and data analysis. The paper was written jointly by L.S., H-H.W., Q-H.W. and S.H.P. All authors have discussed the results and the interpretation.

Additional information

The authors declare no competing financial interests. Supplementary information accompanies this paper on www.nature.com/naturephysics. Reprints and permissions information is available online at http://npg.nature.com/reprintsandpermissions. Correspondence and requests for materials should be addressed to L.S. or H-H.W.

© 2011 Macmillan Publishers Limited. All rights reserved